

The ω^3 scaling of the vibrational density of states in quasi-2D nanoconfined solids

Yuanxi Yu¹, Matteo Baggio^{2†,*}, Chenxing Yang^{1†}, Anthony E. Phillips³, Alessio Zacccone^{4,5‡}, Lei Zhang⁶, Ryoichi Kajimoto⁷, Xiaran Miao⁸, Dehong Yu⁹, and Liang Hong^{1,10,§}

¹School of Physics and Astronomy, Shanghai Jiao Tong University, Shanghai 200240, China.

²Wilczek Quantum Center, School of Physics and Astronomy, Shanghai Jiao Tong University, Shanghai 200240, China & Shanghai Research Center for Quantum Sciences, Shanghai 201315.

³School of Physics and Astronomy, Queen Mary University of London, U.K.

⁴Department of Physics “A. Pontremoli”, University of Milan, via Celoria 16, 20133 Milan, Italy.

⁵Cavendish Laboratory, University of Cambridge, CB3 0HE, Cambridge, U.K.

⁶School of Material Science and Engineering, Shanghai Jiao Tong University, Shanghai 200240, China.

⁷J-PARC Center, Japan Atomic Energy Agency (JAEA), Tokai, Ibaraki, 319-1195, Japan

⁸Shanghai Synchrotron Radiation Facility, Shanghai Institute of Applied Physics, Chinese Academy of Sciences, Shanghai, 201204, China

⁹The Australian Nuclear Science and Technology Organisation, Lucas Heights, NSW 2232, Australia

¹⁰Institute of Natural Sciences, Shanghai Jiao Tong University, Shanghai 200240, China.

*Corresponding author: b.matteo@sjtu.edu.cn

†Co-first author

‡e-mail: alessio.zacccone@unimi.it

§e-mail: hongl3liang@sjtu.edu.cn

ABSTRACT

Atomic vibrations play a vital role in the functions of various physical, chemical, and biological materials. The vibrational properties and the specific heat of a bulk material are well described by the Debye theory, which successfully predicts the quadratic ω^2 low-frequency scaling of the vibrational density of states (VDOS) in bulk solids from few fundamental assumptions. However, the corresponding relationships for nanoconfined materials with fewer degrees of freedom have been far less well explored. In this work, using inelastic neutron scattering, we characterize the VDOS of amorphous ice confined to a thickness of ≈ 1 nm inside graphene oxide membranes and we observe a crossover from the Debye ω^2 scaling to a novel and anomalous ω^3 behaviour upon reducing the confinement size L . Additionally, using molecular dynamics simulations, we not only confirm the experimental findings but also prove that such a novel scaling of the VDOS appears in both crystalline and amorphous solids under slab-confinement. Finally, we theoretically demonstrate that this low-frequency ω^3 law results from the geometric constraints on the momentum phase space induced by confinement along one spatial direction. This new physical phenomenon, revealed by combining theoretical, experimental and simulations results, is relevant to a myriad of systems both in synthetic and biological contexts and it could impact various technological applications for systems under confinement such as nano-devices or thin films.

Introduction

Describing the vibrational and thermodynamic properties of matter is one of the long-standing tasks of solid state physics¹. In the case of bulk solids, the problem has been solved long-time ago, in 1912, by Peter Debye with his celebrated model². Debye’s theory correctly predicts the quadratic $\sim \omega^2$ low-frequency scaling of the vibrational density of states (VDOS) of bulk solids and the corresponding $\sim T^3$ low-temperature scaling of their specific heat, in perfect agreement with many experimental observations^{1,3}. The success was not only achieved on crystalline materials but also on disordered solids as long as the studied frequency is low enough, i.e. much below the infamous boson peak anomaly, and the length scale investigated is above that of structural heterogeneity⁴⁻⁶.

The Debye model relies only on two fundamental assumptions: (I) the low-energy vibrational dynamics is governed by a

set of propagating Goldstone modes⁷, i.e. acoustic phonons, with linear dispersion relation $\omega = v k$ and (II) the phase space for the allowed wave-vectors is given by a perfect spherical manifold of radius k_D , the Debye wavevector. The first assumption is notably violated in liquids in which the late-time (low energy) dynamics is dominated by diffusion⁸, which induces a constant contribution to the density of states observed both in molecular dynamics simulations and in experiments. Additionally, in liquids, normal modes coexist at low energy with a large number of instantaneous normal modes (INMs) which appear as negative eigenvalues of the Hessian or dynamical matrix and they reflect the presence of numerous saddle points in the highly anharmonic potential landscape^{9–11}. Consequently, even when the diffusive contribution is neglected, the density of states in liquids grows linearly with the frequency instead of quadratically as predicted by Debye theory^{12–14}. At the same time, the specific heat does not grow with temperature but rather decreases¹⁵. Both these peculiar behaviours, which remarkably deviate from Debye's theory, can be explained from first principles in terms of instantaneous normal modes^{14,16}. As the system becomes solid, the density of INMs drops to zero and the Debye spectrum is recovered¹⁷. In a nutshell, paraphrasing Stratt¹⁰, the deviations from Debye's theory in liquids are simply due to the fact that "*liquids are not held together by springs*", and strong anharmonicities play a dominant role. Even glasses, despite their well known anomalies¹⁸, display low-energy phonon modes and they indeed respect Debye theory, $g(\omega) \sim \omega^2$, at sufficiently low frequency (lower than the boson peak excess¹⁹). However, whether the Debye model, and indeed even the continuum theory of elasticity, can work in solids under spatial confinement is largely unknown.

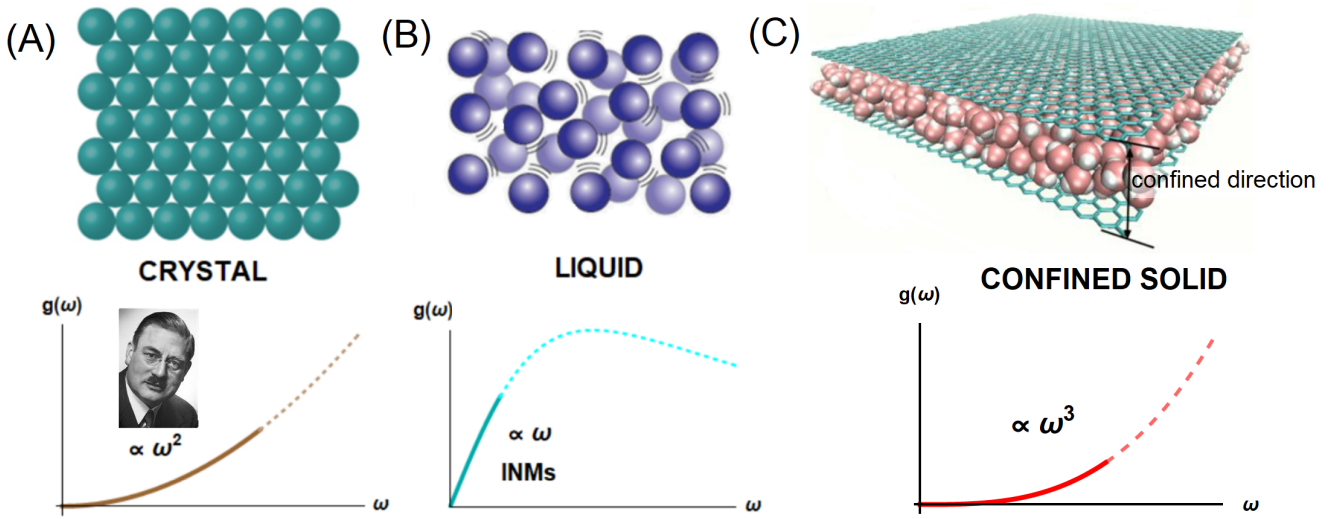


Figure 1. The (low frequency) vibrational density of states $g(\omega)$ for ordered crystalline/amorphous solids with long-range order (A), liquids (B) and slab-confined solids (C). Solids, at low frequency, display a characteristic ω^2 scaling as predicted by Debye theory. Liquids, once the diffusive contribution is removed, shows a peculiar linear scaling due to the presence of instantaneous normal modes. As demonstrated in this work, slab-confined solids, whether amorphous or ordered, exhibits a novel ω^3 scaling which is visible both in experiments and simulations and it can be explained analytically by considering simple geometric constraints on the momentum phase space of low-energy phonon modes.

Nanometer confinement is ubiquitous in the frontiers of bio-technology, electronic engineering and material sciences to achieve unprecedented advantage, e.g., applications of graphene or graphene-based materials for electron conduction^{20–22}, sea water desalination^{23–25} and biosensing^{26–28}. The atomic vibrations in such confined environment plays a crucial role in a plethora of phenomena, such as facilitating electron conduction in graphene-based electronic devices^{29–31}, enhancing proton delivery through the ion channel across the cell membrane^{32–35}, and conduction of energy to power enzymatic motion in protein molecules^{36–39}. The effects of strong confinement have been investigated in nanoconfined liquids^{40–51} where liquid-to-solid transitions have been found^{52–56}. The effects of confinement (specially in nanopores geometries with confinement along two spatial directions) on the VDOS of glasses has been discussed in^{57–66} with particular attention to the fate of the Boson Peak anomaly and glassy relaxational dynamics. Although the importance of reduced dimensionality to nanoscience has long been appreciated, many previous vibrational studies have focused on 0D or 1D confinement in nanopores. To the best of our knowledge, the effects of nano-confinement on the VDOS of solids confined in slab geometries have not been considered so far.

In this work, we performed both inelastic neutron scattering and molecular dynamics simulations on confined crystalline and amorphous ice where the length scale of confinement can be well controlled and span from 7 Å to 2 nm. We found that the

low-energy vibrations of the confined solid scales as a robust $\sim \omega^3$ power law, faster than the expected $\sim \omega^2$ Debye's law. We further show with a simple analytical model that the deviation from Debye's law arises from the effects of the geometrical constraints on the available momentum phase space without changing of the nature of the low-energy excitations, which are still well-described by propagating plane waves $\omega = vk$ as demonstrated also by auxiliary molecular dynamics simulations. Despite similar studies⁵⁷⁻⁶⁶ claiming a low-energy suppression of the VDOS due to confinement have been performed in nano-confined amorphous systems, this novel scaling and its theoretical foundations have been never mentioned nor discussed in the past. Part of the reason, it is that this novel property is peculiar of slab geometries whereas most of the previous literature has been focused on nanopores geometries in which the Debye's law keeps working well at low frequencies.

Experimental evidence

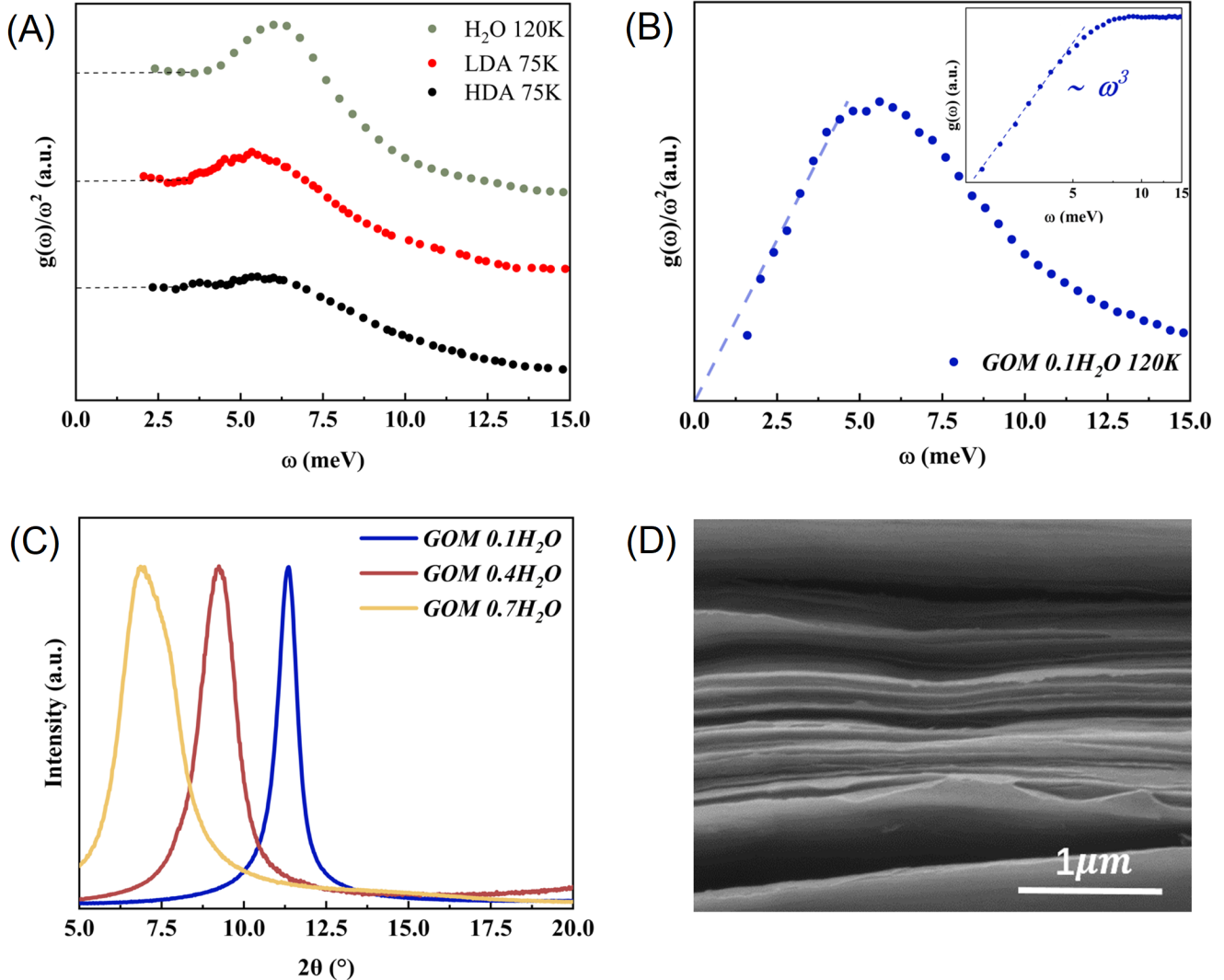


Figure 2. (A): The Debye normalized VDOS $g(\omega)/\omega^2$ for High Density Amorphous (HDA) ice, Low Density Amorphous (LDA) obtained from Ref.⁶ and bulk crystalline ice measured in this work at 120K. The horizontal dashed lines indicate the Debye level at low frequency. The curves have been manually shifted vertically for better presentation and the vertical axes has arbitrary units. (B): The experimental normalized VDOS $g(\omega)/\omega^2$ for the hydrated GOM sample at $h = 0.1$ gram water/gram GOM. The dashed line indicates the low frequency $\sim \omega^3$ novel scaling due to confinement. The inset shows the original VDOS data in log-log scale. The $y-$ axes are presented in arbitrary units. (C): The XRD data of GOM sample with different hydration levels. (D): The scanning electron microscope (SEM) image of the GOM sample which highlights the fuzzy boundaries of the graphene oxide membranes.

Using inelastic neutron scattering, we have measured the VDOS of water at 120 K (ice) confined between graphene oxide

membranes (GOM) with different levels of hydration. The detailed information on the sample preparation, the experimental methods and the data analysis is provided in the Methods.

As a reference, we present the inelastic neutron scattering data of the bulk crystalline ice measured in this work and those for bulk High-density amorphous ice (HDA) and bulk low-density amorphous ice (LDA) ice from Ref.⁶ without confinement in Fig.2 (A). As can be seen, at low frequency, approximately below 4 meV, we observed a leveling-off of the reduced density of state, $g(\omega)/\omega^2$, to a well-defined Debye level, in agreement with the standard Debye model expectation $g(\omega) \sim \omega^2$. This is further supported by the DOS of bulk crystalline ice and disordered one derived from MD simulations (see next Section). Hence, the Debye model is valid for low-energy vibrations in bulk solids without confinement as expected. In sharp contrast, in the sample with lowest amount hydration (0.1 gram water per gram GOM), where the distance between neighboring GOM layers is only 7Å (Fig.2 (C)), the reduced density of states displays a neat low frequency linear scaling, thus the original VOS should scale as $g(\omega) \sim \omega^3$ (Fig.2 (B)). The same feature is shown in a logarithmic plot in the inset of Fig.2 (B). This cubic regime appears robust in a large range of frequencies from ≈ 1.6 meV to ≈ 5 meV. The spectra lower than 1.6 meV are affected by the resolution function of the instrument (0.35 meV upwards to 1meV or so⁶⁷) and thus not presented. In order to make sure that this anomalous scaling does not stem from the GOM structure itself, we measure the VDOS of the dry GOM without any water (shown in Fig.3 (A)). The resulting reduced VDOS, presented in Fig.3 (A), is almost a constant which slowly decreases with frequency. Based on the dependence of reduced VDOS on ω and the absolute amplitude of the dry sample, one can deduce that the observed anomalous ω^3 scaling in hydrated GOM must result from the nano-confined ice sample. Further Neutron Diffraction measurement reveals that the water confined in GOM at this hydration level is amorphous packed as no characteristic Bragg peak of the crystalline ice is present (see Fig.3 (C)). At such low temperature, the translational motion of water molecules should be strongly suppressed like in solids. Thus we name these confined supercooled water molecules without translational freedom as confined amorphous ice.

To further explore this novel ω^3 scaling found in the experimental data, we measured a series of samples with different levels of hydration. The results of the VDOS measurements on the various samples is shown in Figs. 3 (A-B). A lower hydration level corresponds to a smaller confinement size in the vertical z direction, where the inter-layer distance inside the membrane can be varied from 7Å to a few nanometers when increasing h from 0.1 to 0.7. As shown in Fig.3 (B-D), the power law of the low-energy VDOS changes gradually from 3 to 2 when varying $h = 0.1$ to 0.7. Such change of the power law can be rationalized by the following mechanism. When the hydration level is low, the water molecules are mostly confined between GOM layers and form a disordered solid phase; with the increase of h , some water migrates away from being nano-confined between the layers to some large voids or even to the external surface of the GOM to form bulk crystalline ice, namely *ice segregation*⁶⁸⁻⁷⁰. This behaviour is supported by the small-angle X-ray scattering results (see SI). As seen in Fig.3 (C), when the hydration is low, ($h = 0.1$), one can not see any Bragg peaks for hexagonal ice. However, these ice Bragg peaks appear when h is above 0.4. We note that these Bragg peaks are rather narrow, which indicate that they result from bulk crystals instead of nanometer sized crystals, as the latter will significantly broaden the peaks as seen in⁷¹⁻⁷⁴. This is further supported by DSC measurement, where no first-order transition is observed at $h = 0.3$, but it appears at higher hydration levels, $h = 0.4$ or above. Moreover, as evident by SAXS data (see SI), at the high hydration levels (e.g., $h = 0.7$), the interlayer-distance of GOM is suddenly reduced when cooling to 253K at which the Bragg peaks of ice appears. Hence, the bulk ice is formed at high hydration, e.g. $h = 0.4$ and $h = 0.7$, maybe in some large voids or the external surface, not in between GOM layers, otherwise the inter-layer distance should increase rather than decrease as observed. Therefore, one can deduce that the ice formed in each GOM sample is composed by both nano-confined amorphous ice and large bulk crystals. The relative ratio can be estimated using the DSC data (see SI) and the results are presented in Fig.3 (D). As the nano-confined component obeys ω^3 (assumed to be the same as the one discovered at $h = 0.1$) while the bulk crystal follows the Debye's law ω^2 , the final power law should pass gradually from 3 to 2 by smoothly increasing h from the strictly confined case towards the one dominated by the bulk crystal (see Fig.3 (B-D)). The vanishing of the Debye contribution coming from the bulk crystal component is even clearer in the reduced VDOS presented in Fig.3 (A). This agreement supports our previous argument that the density of states of the confined amorphous ice obeys a novel power-law $\sim \omega^3$.

Before moving on, let us comment on another interesting outcome of our experimental analysis. The bulk sample at 120 K displays a sharp resonance peak in the reduced VDOS at ≈ 7 meV (Fig.3 (A)). This peak is attributed to the presence of a specific optical mode of the ice crystal⁷⁵⁻⁷⁷. By decreasing the level of hydration, and therefore increasing the strength of confinement, we observe a shift of this peak towards lower frequencies and a broadening of its linewidth. This observation suggests that the effects of confinement decrease the lifetime of this mode and renormalize the energy of the optical modes similarly to what disorder or anharmonicity would do. Indeed, one could argue that confinement is itself a source of anharmonicity.

Universality of the phenomenon checked with MD simulations at 120 K

In order to confirm the universality of this novel power-law $\sim \omega^3$ for nano-confined solids and to prove that, as expected, it is not a peculiar property of the confined amorphous state, we perform all-atom molecular dynamics (MD) simulations on bulk

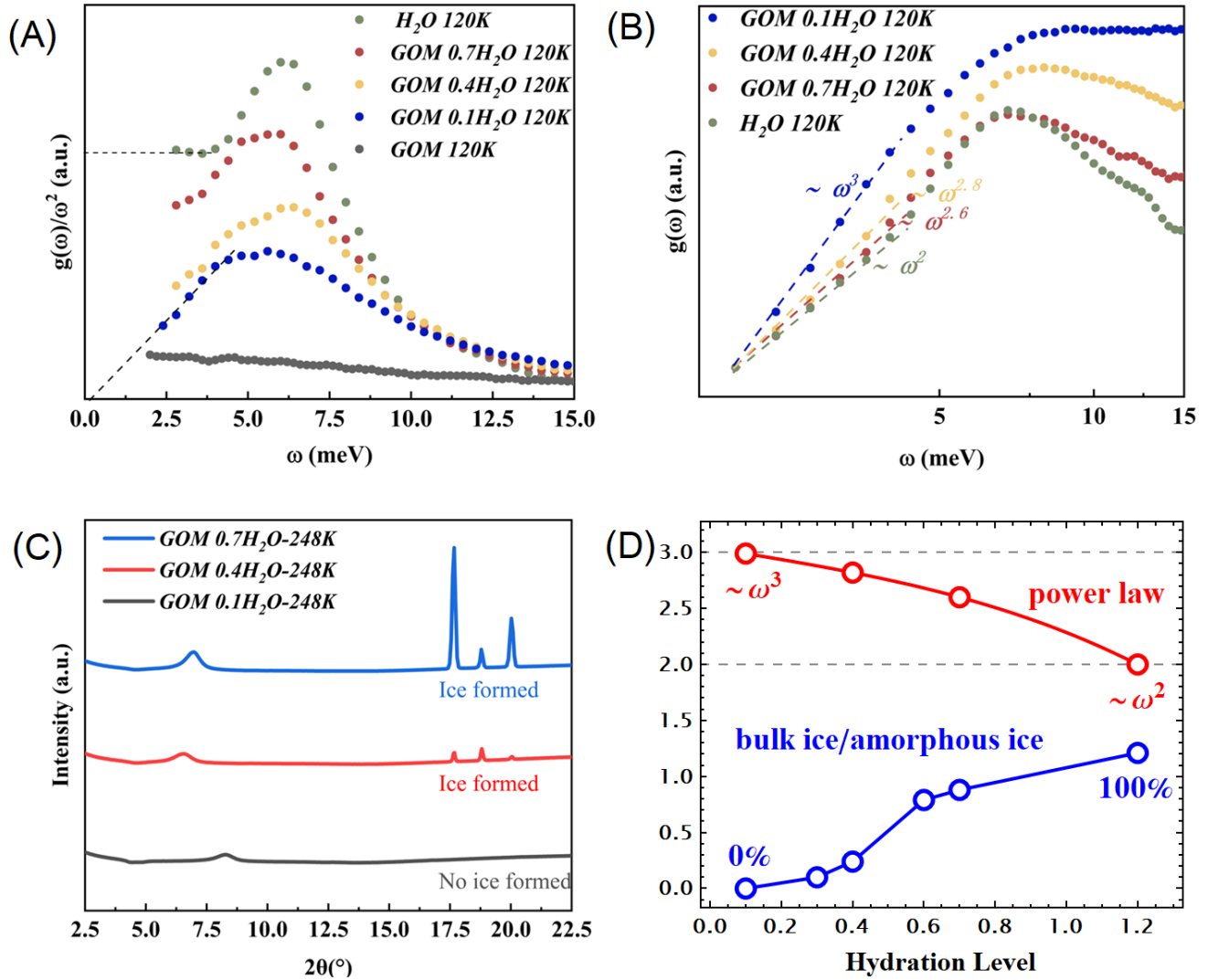


Figure 3. (A): The experimental VDOS normalized by ω^2 vs. frequency for bulk ice (green), GOM sample at $h=0.7$ (red), 0.4 (yellow), 0.1 (blue) respectively, and the dry GOM (gray). The horizontal dashed line guides the eyes towards the Debye level for the bulk sample. The diagonal dashed line guides the eye towards the $g(\omega) \sim \omega^3$ low frequency scaling. The blue data correspond to those reported in the right panel of Fig.2. (B): The original non-normalized VDOS corresponding to the data in panel (A). (C): The neutron diffraction data for samples at different hydration levels. (D): The fitting power of the low frequency VDOS data for different hydration levels (red). The dashed lines indicate the novel ω^3 scaling and the standard quadratic Debye's law. The DSC data showing the mass ratio between bulk and amorphous ice for the corresponding hydration levels (blue).

ice, slab ice, supercooled water and slab supercooled water at 120 K. The different structure between the hexagonal crystalline ice and the amorphous ice is highlighted in the panels (A) and (B) of Fig.4. The geometry of the slab sample is shown in panel (C) of Fig.4. As the slab is of 3 nm along the z direction, and the temperature studied is low enough to freeze the translational freedom of water, the supercooled water can be thus considered as amorphous ice. The details of the simulations can be found in the Methods. The results of the simulations are shown in Fig.4 (D). Both the amorphous and crystalline ices in the bulk phase show a very clear leveling-off of the reduce density of states at low frequency, signaling the presence of a strong Debye scaling law, $g(\omega) \sim \omega^2$. The Debye level is reasonably lower in the crystalline sample as compared to the bulk amorphous case because of a much larger value of the speed of sound. In the slab (confined) samples (see Methods for more details), the VDOS from the simulations shows clear differences in the low frequency behaviour as compared to the bulk sample; the Debye leveling-off is absent and the novel ω^3 scaling shows up, consistent with the neutron scattering experimental findings. In summary, the

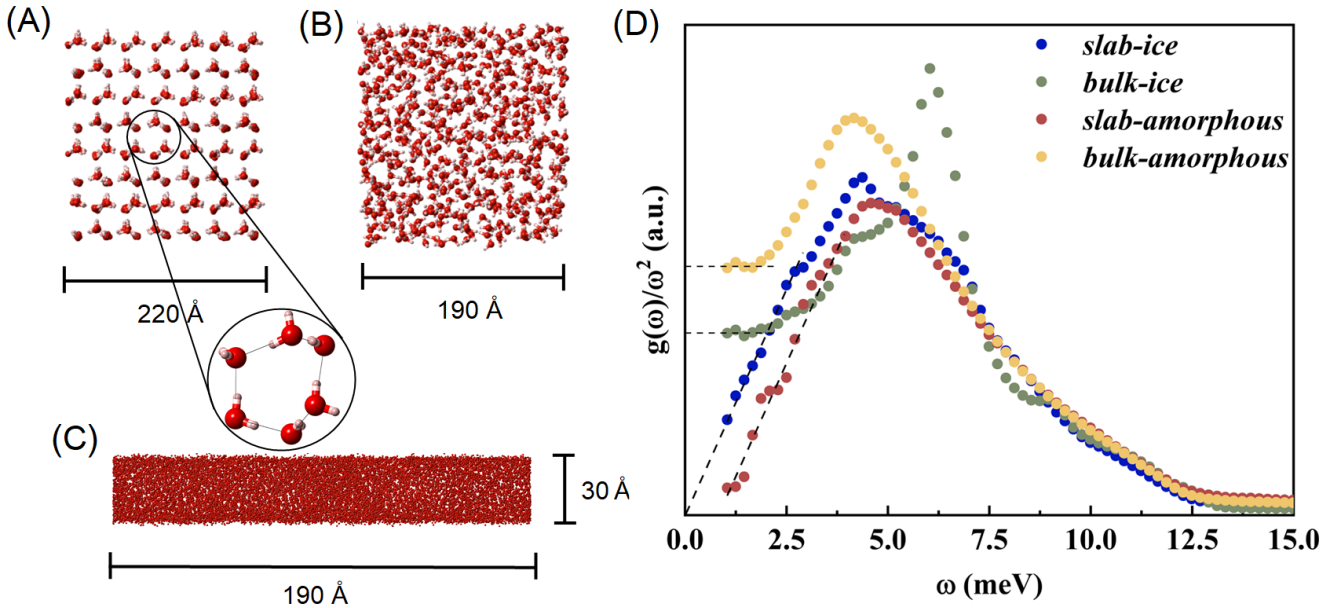


Figure 4. The MD simulations performed at 120 K. **(A):** The snapshot of the bulk ice sample with size 220 Å. For visual purposes, only few layers are kept. The zoom emphasizes its hexagonal structure. **(B):** The snapshot of the bulk amorphous ice sample with size 190 Å. Also here, only few layers are kept. **(C):** The amorphous ice slab sample with size 190 Å and confinement length along the z direction 30 Å. Here, the original structure is kept. **(D):** The normalized VDOS in function of frequency obtained from the MD simulations for slab ice (blue), bulk crystalline ice (green), slab amorphous (red) and bulk amorphous ice (yellow). The horizontal dashed lines indicates the Debye level for the bulk systems. The diagonal dashed lines guide the eyes towards the $g(\omega) \sim \omega^3$ low frequency scaling. The y-axes is presented in arbitrary units.

analysis of the MD simulations not only confirms the outcomes of the experiments, but it also provides more evidence for the universality of the phenomenon which does attain to any confined solids regardless of its crystalline or amorphous structure.

Theoretical explanation

In this section, we provide a concise analytic derivation of the novel ω^3 scaling observed for nano-confined solids both in the experimental data and MD simulations. Let us consider a 3-dimensional system of linear size L . If the system were confined by atomically smooth and infinitely rigid boundaries (which is not the case for our experimental setup, see Fig. 2 (D)), hard-wall boundary conditions (BCs) would apply, implying a net zero displacement of the systems' atoms/molecules near the boundary. In turn, the hard-wall BCs would lead to the usual “quantization” of the wavevector of the acoustic (elastic) waves that can propagate in the system: these are standing waves (eigenmodes of the wave equation) with $k = n\pi/L$, with n being an integer (see SI for more details).

In our system, however, the smooth hard-wall BCs do not apply because the confining boundaries are graphene oxide sheets, in which the basal plane is highly screwed and possesses different and spatially-random-distributed oxide groups (hydroxyl, epoxy, and carboxy groups) (see the scanning electron microscope (SEM) image in Fig. 2 (D)). An additional proof of this fact is provided in the Supplementary material using the MD simulations.

A crucial consequence of the lack of hard-wall BCs is the fact that the minimum wavevector is not $k = \pi/L$ and that the wavevector is not discrete but continuous. We have verified that this is true in the numerical simulations, where it was found that the minimum wavevector is $\approx \frac{1}{4} \frac{\pi}{L}$, as shown in the SI, indeed smaller than π/L and no sign of discreteness was observed either. Similar conclusions about the fundamental role of the boundary conditions in nano-confined systems have been reached in^{57,58}.

Going back to the topic, the number of states with wave-number between k and dk , *i.e.* in a spherical shell in k -space, are given by:

$$dn = V_k 4\pi k^2 dk. \quad (1)$$

where $V_k = (2\pi)^3/L^3$ is the k -state volume occupied by a single wave-vector. Assuming a linear low-energy dispersion relation for the vibrational modes $\omega = v k$, which as we will see persists even at high level of confinement (see SI), one finally obtains

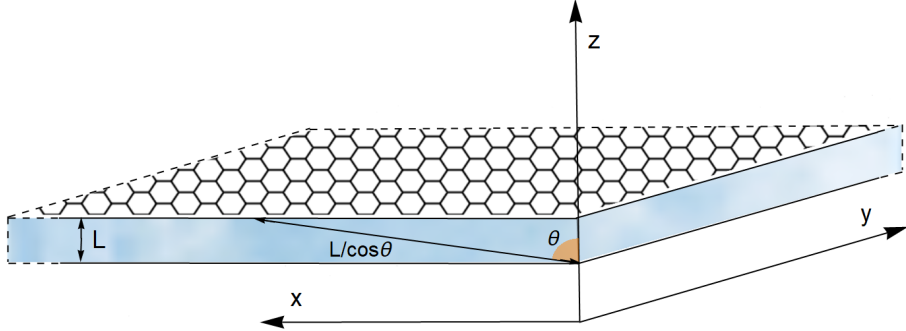


Figure 5. The confined geometry considered. The system size in the (x, y) directions is much larger than that in the z direction, $L_z \ll L_x, L_y$. The system is assumed to be rotational invariant in the 2-dimensional (x, y) subspace. Defining the angle θ with respect to the vertical z axes, the maximum allowed wavelength in that direction is given by $\lambda = L/\cos\theta$. Importantly, the smooth hard-wall boundary conditions are not applicable to our setup.

the density of states as:

$$g(\omega) = g(k) \frac{d\omega}{dk} = \frac{1}{V_k} \frac{dn}{dk} \frac{d\omega}{dk} \sim \omega^2, \quad (2)$$

where we omitted the prefactor since it is undetermined due to the non-smooth BCs. However, the ω^2 scaling coincides with the famous Debye's result^{1,3}. Here, we have considered a single sound mode and we have neglected the existence of different polarizations as in realistic solids. Given the additive property of the density of states $g(\omega)$, we can easily implement this last step by simply summing the contribution from the different polarizations as:

$$g(\omega) \approx \sum_p \omega^2 \quad (3)$$

where p is the index labelling the polarizations. Importantly, the Debye derivation relies on an integration over all directions in the solid angle, reflected in the factor 4π in the above Eq.(3).

Let us now turn to a different situation in which one of the three bulk dimensions is confined but the atoms still free to vibrate along it. This corresponds exactly to the setup considered in the experimental and simulation parts discussed above. We follow closely the framework presented in⁷⁸, and we shall work without hard-wall BCs consistent with the discussion above. In particular, let us consider a geometry which is rotational invariant in the (x, y) plane but in which the z direction is confined in a range $z \in [0, L]$. We assume the size of the sample in the (x, y) direction to be much larger than that in the z direction, $L_z \ll L_x, L_y$. In this case, the minimum wave-vector allowed is given by $2\pi\cos\theta/L$, where θ is the polar angle between the wave-vector and the z direction (see Figure 5)⁷⁸. In the non-confined direction, *i.e.* for $\theta = \pi/2$, the macroscopic geometry does not provide any large-distance cutoff and the minimum value of k is simply zero ($L \rightarrow \infty$). Importantly, this minimum condition does not arise from the hard-wall BCs but simply from the geometry of the slab sample.

As a result of this geometric constraint on k -space, the integration over the polar angles, which gave the 4π factor in Eq.(1), is now replaced by:

$$\int_{\cos^{-1}(Lk/2\pi)}^{\pi/2} \sin\theta d\theta \int_0^{\pi/2} d\phi = 2Lk \quad (4)$$

where the complete integral in the ϕ angle reflects the $SO(2)$ rotational invariance in the (x, y) plane. We note that the expression in Eq.(4) reduces to the standard result when the wave-vector approaches the value $k = 2\pi/L$. In particular, in that limit, the lower limit of integration tends to zero. Hence, we now obtain that the number of states with wavenumber in the range $\in [k, k + dk]$ is given by:

$$dn \sim Lk^3 dk. \quad (5)$$

which clearly deviates from the Debye result. In Eq.(5), the numerical pre-factors have been neglected since they are not relevant for the present analysis. Following the same steps as before, one can deduce the VDOS at low frequency as:

$$g(\omega) \sim \omega^3 \quad (6)$$

which is our main result of this section.

Eq.(6) predicts a fundamental deviation from the Debye $\sim \omega^2$ law which arises because of the geometric constraints on the momentum phase space induced by spatial confinement in real space. This simple analysis is in perfect agreement with the experimental and simulations outcomes of the previous sections and it is able to explain in a simple language the novel ω^3 universal scaling in solid systems under slab-confinement. Importantly, the same results would not be obtained for geometries with confinement along two spatial directions (cylinder) or three spatial directions (sphere) where, at least at low frequency, the Debye's law is expected to work, as also confirmed in^{57,61-64,66}.

Conclusions

In this work, we have reported the experimental observation of a low frequency anomalous scaling in the vibrational density of states of nano-confined solids which violates the well-known Debye's law for bulk solid systems. In particular, using inelastic neutron scattering experiments on an amorphous ice sample at 120 K nano-confined inside graphene oxide membranes, we have observed a novel low-frequency ω^3 scaling law which substitutes the quadratic behaviour expected from Debye theory. This interesting experimental finding was further confirmed by all-atom molecular dynamics simulations on confined ice in both crystalline and amorphous phases. Finally, using a simple geometric argument, we derived a generalized law for the vibrational density of states of systems confined along one spatial direction, and we have proved analytically the appearance of this novel scaling as a consequence of a restricted momentum phase space due to the geometric constraints imposed by confinement, while the nature of the low-energy vibrational modes remain propagating acoustic waves. Our picture is perfectly compatible with the idea that strong confinement produces a depletion of the low-energy part of the VDOS spectrum observed in several amorphous systems confined in nanopores^{58,60,61,64,66}, where nevertheless Debye's law is still obeyed at low frequencies.

Our analysis provides a universal answer to the fundamental question of the vibrational properties of nano-confined solids and it paves a new path towards the understanding and study of the mechanical properties of condensed matter systems under confinement⁷⁹⁻⁸¹. A direct consequence of this ω^3 scaling in VDOS is to shift the acoustic modes towards the higher energies. Thus, the phonon-assisted transportation of energy, electron or proton in various electronic devices and biological systems of nano-meter confinement will be inevitably carried out more by the high-energy short-wavelength phonon modes. More specific functional changes of materials due to this new mechanism are left to be discovered. They may be significant to fields including nano-mechanical systems and transport phenomena at the nano-scale to the nano-scale manipulation of biological systems.

Methods

Sample preparation. The GOM sample was synthesized using the modified Hummers' method.⁸² The GOM sample was first dehydrated by heating it from room temperature to 40 °C and then annealed at this temperature for 12 h in a vacuum to the dry condition. The oxidation rate of the GOM sample is 28%, which is determined by XPS. The dehydrated sample was sealed in a desiccator and exposed to the water vapor to allow water molecules to adsorb to the surface and the interlamination of the GOM sheets. The hydration levels were controlled by adjusting the expose time of the sample and the final values of hydration levels were determined by measuring the weight before and after the water adsorption.

Differential Scanning Calorimetry (DSC). Differential scanning calorimetry (DSC) was used to measure the ratio between bulk ice and confined amorphous ice in GOM sample at low temperature. The DSC results of GOM at different hydration levels were performed by the DSC1 (METTLER TOLEDO). The samples were first annealed at 20°C for 5 minutes, and then cooled down to -60 °C at a cooling rate of 2°C/min to obtain the DSC data (see SI). The DSC data were analyzed by the TA Trios software.

Powder X-ray Diffraction (PXRD). The powder X-ray diffraction data for GOM at different hydration levels were collected using a Rigaku Mini Flex600 X-ray diffractometer, with a Cu K α source ($\lambda = 1.5406 \text{ \AA}$) operated at 40kV and 15 mA at a scan rate of 10°/min from 10° to 60°. The PXRD data were analyzed by MDI Jade software.

Small Angle X-ray Scattering (SAXS). SAXS characterizations were employed to monitor the interlayer distance evolution in GOM with temperature decreasing and ice freezing. The SAXS measurements were carried out at the BL16B1 beamline of the Shanghai Synchrotron Radiation Facility (SSRF). The wavelength of the X-ray was 1.24 \AA . The SAXS patterns were collected by using a Pilatus 2M detector with a resolution of 1475 pixels \times 1679 pixels and a pixel size of $172 \mu\text{m} \times 172 \mu\text{m}$. The data acquisition time for SAXS was set as 10 s for each frame. The sample-to-detector distances of the SAXS is 258mm, respectively

Scanning Electron Spectroscopy (SEM). SEM images were taken by a MIRA 3 FE-SEM with a 5 kV accelerating voltage.

Neutron Scattering. The dynamic neutron scattering is described in terms of the intermediate scattering function, $I(\mathbf{q}, t)$ including incoherent and coherent terms $I_{inc}(\mathbf{q}, t)$ and $I_{coh}(\mathbf{q}, t)$:

$$I_{inc}(\mathbf{q}, t) = \sum_j^N b_{j,inc}^2 \langle \exp[-i\mathbf{q} \cdot \mathbf{r}_j(0)] \cdot \exp[i\mathbf{q} \cdot \mathbf{r}_j(t)] \rangle, \quad (7)$$

$$I_{coh}(\mathbf{q}, t) = \sum_j^N \sum_i^N b_{j,inc} b_{i,coh} \langle \exp[-i\mathbf{q} \cdot \mathbf{r}_i(0)] \cdot \exp[i\mathbf{q} \cdot \mathbf{r}_j(t)] \rangle, \quad (8)$$

where N is the total number of atoms, $b_{j,inc}$ and $b_{j,coh}$ are the incoherent and coherent scattering lengths of a given atom j , \mathbf{r}_j is the coordination vector of that atom, the bracket $\langle \dots \rangle$ denotes an ensemble and orientation average and \mathbf{q} is the scattering wave vector. $I_{inc}(\mathbf{q}, t)$ contains the information about self-motions of atoms, and $I_{coh}(\mathbf{q}, t)$ probes mostly interatomic motions. As the incoherent scattering cross section of hydrogen is at least one order of magnitude larger than incoherent and coherent scattering cross sections of other elements, the neutron signals collected on GOM hydrated in H_2O are dominated by incoherent intermediate scattering function, $I_{inc}(\mathbf{q}, t)$ and primarily reflect the self-motion of the water molecules. When $t = 0$, the coherent intermediate scattering function, I_{coh} , becomes the static structure factor, $I(\mathbf{q})$, characterizing the atomic structure of the system.

$$I(\mathbf{q}) = \sum_j^N \sum_i^N b_{j,inc} b_{i,coh} \langle \exp[-i\mathbf{q} \cdot \mathbf{r}_i(t_0)] \cdot \exp[i\mathbf{q} \cdot \mathbf{r}_j(t_0)] \rangle \quad (9)$$

The measured dynamic structure factor, $S(\mathbf{q}, \omega)$, is the time Fourier transform of the intermediate scattering function,

$$S_{inc}(\mathbf{q}, \omega) = \int_{-\infty}^{+\infty} I_{inc}(\mathbf{q}, t) \exp(i\omega t) dt, \quad (10)$$

$$S_{coh}(\mathbf{q}, \omega) = \int_{-\infty}^{+\infty} I_{coh}(\mathbf{q}, t) \exp(i\omega t) dt, \quad (11)$$

where ω is the frequency and their product $\hbar\omega = \Delta E$ is the energy transfer between the incident and scattered neutron. $S(\mathbf{q}, \omega)$ furnishes the amplitude-weighted distribution of the dynamic modes in the sample over frequency at a given \mathbf{q} .

Inelastic Neutron Scattering (INS). As the incoherent scattering cross section of hydrogen is at least 1 order of magnitude larger than incoherent and coherent scattering cross sections of other elements, the neutron signals are dominated by incoherent scattering function, and primarily reflect the self-motion of the water molecules. The experimental vibrational density of states (DOS) $g(\omega)$ can be obtained from the dynamic structure factor, $S(\mathbf{q}, \omega)$ using the function⁸³:

$$g(\omega) = \frac{\hbar\omega}{q^2} S(\mathbf{q}, \omega) (1 - e^{-\frac{\hbar\omega}{kT}}) \quad (12)$$

where \hbar is the Planck constant, \mathbf{q} is the scattering wave vector, ω is the frequency which related the energy transfer, k is the Boltzmann constant, and T is the temperature. The experiments for samples of pure water, GOM absorbed by H_2O with h (gram water/gram GOM) of 0.1, 0.4 and 0.7 were conducted by using a time-of-flight (TOF) cold neutron polarization analysis spectrometer PELICAN at ANSTO in AU with an energy resolution $\Delta E = 0.35$ meV (upwards to 1 meV or so⁶⁷) and the energy ranges up to 24.8 meV in the \mathbf{q} range from 0.08\AA^{-1} to 4.5\AA^{-1} . The incident energy is 14.2 meV with wavelength of 2.4\AA . The samples were contained inside aluminum foils in a solid form and sealed in aluminum sample cans in a helium atmosphere. The data were converted from raw Time-of-Flight to energy transfer with the energy incident on the sample calculated from the monitors before and after the sample position. The empty can signal was subtracted at each temperature. The detector efficiency in the data was normalized using a vanadium standard. All steps were performed with standard routines within the LAMP software package⁸⁴ and the scripts are available upon request. The experiment for pure dry GOM was conducted by using a high-intensity Fermi-chopper spectrometer 4SEASONS at JPARC in Japan with an energy resolution $\Delta E = 1.2$ meV and energy range up to 17.2 meV in the \mathbf{q} range from 0.225\AA^{-1} to 7\AA^{-1} . The measurement was done with multi-incident energy and the data with incident energy 27.128 meV was chosen to get the best resolution. Similar processing steps to other samples data above were performed on Mslice software package.

Molecular dynamics (MD) simulation. The MD simulations were performed using LAMMPS⁸⁵ to simulate ice and supercooled water at 120 K. The supercooled water is simply obtained by simulating bulk liquid water at room temperature and then

cooled down to 120 K. A temperature of 120 K is low enough to freeze out the translational degrees of freedom, therefore one can consider the disorderly-packed water at such temperature as amorphous ice. The equilibration of MD systems was performed in constant-temperature and constant pressure ensemble, using the Nosé-Hoover thermostat and Parrinello-Rahman barostat to control the temperature and pressure, and then switched to NVT ensemble to calculate dynamical properties. The timestep is set as 2 fs. The inter-molecule potential of H_2O is TIP4P/2005⁸⁶, which shows good accuracy for ice and supercooled water⁸⁷. To reduce the finite-size effect, the simulation are performed using 360,000 and 216,000 molecules for ice and disorderly respectively, with the configuration edge sizes of 180 and 200 Å. Both crystal and amorphous structures were equilibrated at 120 K at 1 atm. The slab structures were then cut from the bulk system with 30 Å thickness. We freeze the bottom and top layer (~3 Å) of the slab systems to force the structure remain 2-d confined during the following simulation. To find the optimal volume of the ice slab, we performed simulation for ice slab in the NPT ensemble. The position of the top and bottom layer were re-scaled to new positions when the simulation box changes. A snapshot of the slab geometry can be found in Fig. 4 (C) in the main text.

The VDOS is calculated by the Fourier transform of the oxygen velocity autocorrelation function:

$$C_v(\omega) = \int_{-\infty}^{\infty} C_v(t) \exp(-i\omega t) dt, \quad (13)$$

and the velocity auto-correlation function (VAF) is defined as:

$$C_v(t) = \langle \vec{v}(0) \cdot \vec{v}(t) \rangle \quad (14)$$

where $\vec{v}(0)$ are the oxygen velocities.

Acknowledgements

We thank Reiner Zorn and Jie Zhang for useful discussions.

We also appreciate the assistance from Instrumental Analysis Center of Shanghai Jiao Tong University for SEM, PXRD, DSC measurements. M.B. acknowledges the support of the Shanghai Municipal Science and Technology Major Project (Grant No.2019SHZDZX01). C. Y. acknowledges the support of the NSF China (11904224). This work was supported by NSF China (11504231, 31630002 and 22063007), the Innovation Program of Shanghai Municipal Education Commission and the FJIRSM&IUE Joint Research Fund (No. RHZX-2019-002).

Author contributions

Y.Y. performed the experimental measurements; M.B. and L.H. conceived the idea of this work, C.Y. implemented the MD simulations, L.Z. made the experimental sample, A.E.P., M.B. and A.Z. developed the theoretical model; R.K. and D.Y. helped with the neutron scattering experiments in the Japan and Australia, respectively; X.M. helped with the X-ray diffraction data collection and analysis. All the authors contributed to the writing of the manuscript.

Competing interests

The authors declare that no competing interests exist.

References

1. W. A., Ashcroft, N., Mermin, N., Mermin, N. & Company, B. P. *Solid State Physics*. HRW international editions (Holt, Rinehart and Winston, 1976).
2. Debye, P. Zur Theorie der spezifischen Wärmen. *Annalen der Physik* **344**, 789–839, DOI: [10.1002/andp.19123441404](https://doi.org/10.1002/andp.19123441404) (1912).
3. Chaikin, P. & Lubensky, T. *Principles of Condensed Matter Physics* (Cambridge University Press, 2000).
4. Zorn, R. *et al.* Low frequency vibrational density of state of highly permeable super glassy polynorbornenes—the boson peak. *Phys. Chem. Chem. Phys.* **22**, 18381–18387 (2020).
5. Sangster, M. An introduction to lattice dynamics. *Phys. Bull.* **24**, 305 (1973).
6. Koza, M. M. *et al.* Nature of amorphous polymorphism of water. *Phys. review letters* **94**, 125506 (2005).
7. Leutwyler, H. Phonons as goldstone bosons. *Helv. Phys. Acta* **70**, 275–286 (1997). [hep-ph/9609466](https://arxiv.org/abs/hep-ph/9609466).
8. Hansen, J.-P. & McDonald, I. R. *Theory of simple liquids* (Elsevier, 1990).
9. Zwanzig, R. On the relation between self-diffusion and viscosity of liquids. *The J. Chem. Phys.* **79**, 4507–4508, DOI: [10.1063/1.446338](https://doi.org/10.1063/1.446338) (1983). <https://doi.org/10.1063/1.446338>.

10. Stratt, R. M. The instantaneous normal modes of liquids. *Accounts Chem. Res.* **28**, 201–207, DOI: [10.1021/ar00053a001](https://doi.org/10.1021/ar00053a001) (1995).
11. Keyes, T. Instantaneous normal mode approach to liquid state dynamics. *The J. Phys. Chem. A* **101**, 2921–2930, DOI: [10.1021/jp963706h](https://doi.org/10.1021/jp963706h) (1997).
12. Rabani, E., Gezelter, J. D. & Berne, B. J. Calculating the hopping rate for self-diffusion on rough potential energy surfaces: Cage correlations. *The J. Chem. Phys.* **107**, 6867–6876, DOI: [10.1063/1.474927](https://doi.org/10.1063/1.474927) (1997). <https://doi.org/10.1063/1.474927>.
13. Zhang, W., Douglas, J. F. & Starr, F. W. What does the instantaneous normal mode spectrum tell us about dynamical heterogeneity in glass-forming fluids? *The J. Chem. Phys.* **151**, 184904, DOI: [10.1063/1.5127821](https://doi.org/10.1063/1.5127821) (2019). <https://doi.org/10.1063/1.5127821>.
14. Zaccone, A. & Baglioli, M. Universal law for the vibrational density of states of liquids. *Proc. Natl. Acad. Sci.* **118**, DOI: [10.1073/pnas.2022303118](https://doi.org/10.1073/pnas.2022303118) (2021). <https://www.pnas.org/content/118/5/e2022303118.full.pdf>.
15. Bolmatov, D., Brazhkin, V. V. & Trachenko, K. The phonon theory of liquid thermodynamics. *Sci. Reports* **2**, 421, DOI: [10.1038/srep00421](https://doi.org/10.1038/srep00421) (2012).
16. Baglioli, M. & Zaccone, A. Explaining the specific heat of liquids based on instantaneous normal modes (2021). [2101.07585](https://doi.org/10.1038/srep00421).
17. Bembenek, S. D. & Laird, B. B. Instantaneous normal modes and the glass transition. *Phys. Rev. Lett.* **74**, 936–939, DOI: [10.1103/PhysRevLett.74.936](https://doi.org/10.1103/PhysRevLett.74.936) (1995).
18. Zeller, R. C. & Pohl, R. O. Thermal conductivity and specific heat of noncrystalline solids. *Phys. Rev. B* **4**, 2029–2041, DOI: [10.1103/PhysRevB.4.2029](https://doi.org/10.1103/PhysRevB.4.2029) (1971).
19. Baglioli, M. & Zaccone, A. Universal origin of boson peak vibrational anomalies in ordered crystals and in amorphous materials. *Phys. Rev. Lett.* **122**, 145501, DOI: [10.1103/PhysRevLett.122.145501](https://doi.org/10.1103/PhysRevLett.122.145501) (2019).
20. Otake, K.-i. *et al.* Confined water-mediated high proton conduction in hydrophobic channel of a synthetic nanotube. *Nat. communications* **11**, 1–7 (2020).
21. Liu, J., Shi, G., Guo, P., Yang, J. & Fang, H. Blockage of water flow in carbon nanotubes by ions due to interactions between cations and aromatic rings. *Phys. review letters* **115**, 164502 (2015).
22. Liu, Z. *et al.* Heterogeneity of water molecules on the free surface of thin reduced graphene oxide sheets. *The J. Phys. Chem. C* **124**, 11064–11074 (2020).
23. Chen, L. *et al.* Ion sieving in graphene oxide membranes via cationic control of interlayer spacing. *Nature* **550**, 380–383 (2017).
24. Shi, G. *et al.* Ion enrichment on the hydrophobic carbon-based surface in aqueous salt solutions due to cation- π interactions. *Sci. reports* **3**, 1–5 (2013).
25. Wei, N., Peng, X. & Xu, Z. Understanding water permeation in graphene oxide membranes. *ACS applied materials & interfaces* **6**, 5877–5883 (2014).
26. Borini, S. *et al.* Ultrafast graphene oxide humidity sensors. *ACS nano* **7**, 11166–11173 (2013).
27. Cai, B. *et al.* Ultrasensitive label-free detection of pna–dna hybridization by reduced graphene oxide field-effect transistor biosensor. *ACS nano* **8**, 2632–2638 (2014).
28. Kim, D.-J. *et al.* Reduced graphene oxide field-effect transistor for label-free femtomolar protein detection. *Biosens. bioelectronics* **41**, 621–626 (2013).
29. Brar, V. W. *et al.* Gate-controlled ionization and screening of cobalt adatoms on a graphene surface. *Nat. Phys.* **7**, 43–47 (2011).
30. Zhang, Y. *et al.* Giant phonon-induced conductance in scanning tunnelling spectroscopy of gate-tunable graphene. *Nat. Phys.* **4**, 627–630 (2008).
31. Qiu, X., Nazin, G. & Ho, W. Vibronic states in single molecule electron transport. *Phys. review letters* **92**, 206102 (2004).
32. Jiang, X. *et al.* Resolving voltage-dependent structural changes of a membrane photoreceptor by surface-enhanced ir difference spectroscopy. *Proc. Natl. Acad. Sci.* **105**, 12113–12117 (2008).
33. Ghosh, A., Qiu, J., DeGrado, W. F. & Hochstrasser, R. M. Tidal surge in the m2 proton channel, sensed by 2d ir spectroscopy. *Proc. Natl. Acad. Sci.* **108**, 6115–6120 (2011).

34. Garczarek, F. & Gerwert, K. Functional waters in intraprotein proton transfer monitored by ftir difference spectroscopy. *Nature* **439**, 109–112 (2006).

35. Resler, T., Schultz, B.-J., Lórenz-Fonfría, V. A., Schlesinger, R. & Heberle, J. Kinetic and vibrational isotope effects of proton transfer reactions in channelrhodopsin-2. *Biophys. journal* **109**, 287–297 (2015).

36. Yu, M. *et al.* One-dimensional nature of protein low-energy vibrations. *Phys. Rev. Res.* **2**, 032050 (2020).

37. Leitner, D. M. Energy flow in proteins. *Annu. Rev. Phys. Chem.* **59**, 233–259 (2008).

38. Agarwal, P. K. Role of protein dynamics in reaction rate enhancement by enzymes. *J. Am. Chem. Soc.* **127**, 15248–15256 (2005).

39. Schwartz, S. D. & Schramm, V. L. Enzymatic transition states and dynamic motion in barrier crossing. *Nat. chemical biology* **5**, 551–558 (2009).

40. GRANICK, S. Motions and relaxations of confined liquids. *Science* **253**, 1374–1379, DOI: [10.1126/science.253.5026.1374](https://doi.org/10.1126/science.253.5026.1374) (1991). <https://science.scienmag.org/content/253/5026/1374.full.pdf>.

41. Mandal, S. *et al.* Multiple reentrant glass transitions in confined hard-sphere glasses. *Nat. Commun.* **5**, 4435, DOI: [10.1038/ncomms5435](https://doi.org/10.1038/ncomms5435) (2014).

42. Cummings, P. T., Docherty, H., Iacovella, C. R. & Singh, J. K. Phase transitions in nanoconfined fluids: The evidence from simulation and theory. *AIChE J.* **56**, 842–848, DOI: <https://doi.org/10.1002/aic.12226> (2010). <https://aiche.onlinelibrary.wiley.com/doi/10.1002/aic.12226>.

43. Zhu, Y. & Granick, S. Superlubricity: A paradox about confined fluids resolved. *Phys. Rev. Lett.* **93**, 096101, DOI: [10.1103/PhysRevLett.93.096101](https://doi.org/10.1103/PhysRevLett.93.096101) (2004).

44. Kienle, D. F. & Kuhl, T. L. Density and phase state of a confined nonpolar fluid. *Phys. Rev. Lett.* **117**, 036101, DOI: [10.1103/PhysRevLett.117.036101](https://doi.org/10.1103/PhysRevLett.117.036101) (2016).

45. Gribova, N., Arnold, A., Schilling, T. & Holm, C. How close to two dimensions does a lennard-jones system need to be to produce a hexatic phase? *The J. Chem. Phys.* **135**, 054514, DOI: [10.1063/1.3623783](https://doi.org/10.1063/1.3623783) (2011). <https://doi.org/10.1063/1.3623783>.

46. Franosch, T., Lang, S. & Schilling, R. Fluids in extreme confinement. *Phys. Rev. Lett.* **109**, 240601, DOI: [10.1103/PhysRevLett.109.240601](https://doi.org/10.1103/PhysRevLett.109.240601) (2012).

47. Mandal, S. & Franosch, T. Diverging time scale in the dimensional crossover for liquids in strong confinement. *Phys. Rev. Lett.* **118**, 065901, DOI: [10.1103/PhysRevLett.118.065901](https://doi.org/10.1103/PhysRevLett.118.065901) (2017).

48. Yang, J., Li, Y.-W. & Ciamarra, M. P. Long-wavelength fluctuations and dimensionality crossover in confined liquids (2021). [2107.12225](https://doi.org/10.1103/PhysRevLett.122.2107.12225).

49. Mosaddeghi, H., Alavi, S., Kowsari, M. H. & Najafi, B. Simulations of structural and dynamic anisotropy in nanoconfined water between parallel graphite plates. *The J. Chem. Phys.* **137**, 184703, DOI: [10.1063/1.4763984](https://doi.org/10.1063/1.4763984) (2012). <https://doi.org/10.1063/1.4763984>.

50. Dobrzanski, C. D., Gurevich, B. & Gor, G. Y. Elastic properties of confined fluids from molecular modeling to ultrasonic experiments on porous solids. *Appl. Phys. Rev.* **8**, 021317, DOI: [10.1063/5.0024114](https://doi.org/10.1063/5.0024114) (2021). <https://doi.org/10.1063/5.0024114>.

51. Borghi, F. & Podestà, A. Ionic liquids under nanoscale confinement. *Adv. Physics: X* **5**, 1736949, DOI: [10.1080/23746149.2020.1736949](https://doi.org/10.1080/23746149.2020.1736949) (2020). <https://doi.org/10.1080/23746149.2020.1736949>.

52. Schmidt, M. & Löwen, H. Freezing between two and three dimensions. *Phys. Rev. Lett.* **76**, 4552–4555, DOI: [10.1103/PhysRevLett.76.4552](https://doi.org/10.1103/PhysRevLett.76.4552) (1996).

53. Löwen, H. Twenty years of confined colloids: from confinement-induced freezing to giant breathing. *J. Physics: Condens. Matter* **21**, 474203, DOI: [10.1088/0953-8984/21/47/474203](https://doi.org/10.1088/0953-8984/21/47/474203) (2009).

54. Klein, J. & Kumacheva, E. Confinement-induced phase transitions in simple liquids. *Science* **269**, 816–819, DOI: [10.1126/science.269.5225.816](https://doi.org/10.1126/science.269.5225.816) (1995). <https://science.scienmag.org/content/269/5225/816.full.pdf>.

55. Klein, J. & Kumacheva, E. Simple liquids confined to molecularly thin layers. i. confinement-induced liquid-to-solid phase transitions. *The J. Chem. Phys.* **108**, 6996–7009, DOI: [10.1063/1.476114](https://doi.org/10.1063/1.476114) (1998). <https://doi.org/10.1063/1.476114>.

56. Demirel, A. L. & Granick, S. Origins of solidification when a simple molecular fluid is confined between two plates. *The J. Chem. Phys.* **115**, 1498–1512, DOI: [10.1063/1.1380207](https://doi.org/10.1063/1.1380207) (2001). <https://doi.org/10.1063/1.1380207>.

57. Schönhals, A., Zorn, R. & Frick, B. Inelastic neutron spectroscopy as a tool to investigate nanoconfined polymer systems. *Polymer* **105**, 393–406, DOI: <https://doi.org/10.1016/j.polymer.2016.06.006> (2016). Structure and Dynamics of Polymers studied by X-ray, Neutron and Muon Scattering.

58. Zorn, R. Boson peak in confined disordered systems. *Phys. Rev. B* **81**, 054208, DOI: [10.1103/PhysRevB.81.054208](https://doi.org/10.1103/PhysRevB.81.054208) (2010).

59. Li, D. *et al.* The dependence of the boson peak on the thickness of cu50zr50 film metallic glasses. *Phys. Chem. Chem. Phys.* **23**, 982–989, DOI: [10.1039/D0CP05327A](https://doi.org/10.1039/D0CP05327A) (2021).

60. Cortie, D. L. *et al.* Boson peak in ultrathin alumina layers investigated with neutron spectroscopy. *Phys. Rev. Res.* **2**, 023320, DOI: [10.1103/PhysRevResearch.2.023320](https://doi.org/10.1103/PhysRevResearch.2.023320) (2020).

61. Krause, C., Zorn, R., Frick, B. & Schönhals, A. Thermal properties and vibrational density of states of a nanoconfined discotic liquid crystal. *Colloid Polym. Sci.* **292**, 1949–1960, DOI: [10.1007/s00396-014-3247-3](https://doi.org/10.1007/s00396-014-3247-3) (2014).

62. Zorn, R., Richter, D., Hartmann, L., Kremer, F. & Frick, B. Inelastic neutron scattering experiments on the fast dynamics of a glass forming liquid in mesoscopic confinements. *J. Phys. IV France* **10**, Pr7–83–Pr7–86, DOI: [10.1051/jp4:2000715](https://doi.org/10.1051/jp4:2000715) (2000).

63. Frick, B. *et al.* Inelastic neutron scattering for investigating the dynamics of confined glass-forming liquids. *J. Non-Crystalline Solids* **351**, 2657–2667, DOI: <https://doi.org/10.1016/j.jnoncrysol.2005.03.061> (2005). Proceedings of 3rd International Conference on Broadband Dielectric Spectroscopy and its Applications.

64. Asthalter, T. *et al.* Confined phonons in glasses. *The Eur. Phys. J. E* **12**, 9–12, DOI: [10.1140/epjed/e2003-01-003-7](https://doi.org/10.1140/epjed/e2003-01-003-7) (2003).

65. Carles, R., Benzo, P., Pécassou, B. & Bonafo, C. Vibrational density of states and thermodynamics at the nanoscale: the 3d-2d transition in gold nanostructures. *Sci. Reports* **6**, 39164, DOI: [10.1038/srep39164](https://doi.org/10.1038/srep39164) (2016).

66. Schönhals, A. *et al.* Vibrational and molecular dynamics of a nanoconfined liquid crystal. *The Eur. Phys. J. Special Top.* **189**, 251–255, DOI: [10.1140/epjst/e2010-01329-5](https://doi.org/10.1140/epjst/e2010-01329-5) (2010).

67. Yu, D., Mole, R., Noakes, T., Kennedy, S. & Robinson, R. Pelican—a time of flight cold neutron polarization analysis spectrometer at opal. *J. Phys. Soc. Jpn.* **82**, SA027 (2013).

68. Gutiérrez, M. C., Ferrer, M. L. & del Monte, F. Ice-templated materials: Sophisticated structures exhibiting enhanced functionalities obtained after unidirectional freezing and ice-segregation-induced self-assembly. *Chem. Mater.* **20**, 634–648 (2008).

69. Murton, J. B., Peterson, R. & Ozouf, J.-C. Bedrock fracture by ice segregation in cold regions. *Science* **314**, 1127–1129 (2006).

70. Öberg, K. I., Fayolle, E. C., Cuppen, H. M., van Dishoeck, E. F. & Linnartz, H. Quantification of segregation dynamics in ice mixtures. *Astron. & Astrophys.* **505**, 183–194 (2009).

71. Mancinelli, R. The effect of confinement on water structure. *J. Physics: Condens. Matter* **22**, 404213 (2010).

72. Baker, J., Dore, J. C. & Behrens, P. Nucleation of ice in confined geometry. *The J. Phys. Chem. B* **101**, 6226–6229 (1997).

73. Stefanutti, E. *et al.* Ice crystallization observed in highly supercooled confined water. *Phys. Chem. Chem. Phys.* **21**, 4931–4938 (2019).

74. Morishige, K. & Uematsu, H. The proper structure of cubic ice confined in mesopores. *The J. chemical physics* **122**, 044711 (2005).

75. Schober, H. *et al.* Crystal-like high frequency phonons in the amorphous phases of solid water. *Phys. review letters* **85**, 4100 (2000).

76. Koza, M. M. Vibrational dynamics of amorphous ice structures studied by high-resolution neutron spectroscopy. *Phys. Rev. B* **78**, 064303 (2008).

77. Koza, M., Schober, H., Parker, S. & Peters, J. Vibrational dynamics and phonon dispersion of polycrystalline ice xii and of high-density amorphous ice. *Phys. Rev. B* **77**, 104306 (2008).

78. Phillips, A. E., Baggioli, M., Sirk, T. W., Trachenko, K. & Zacccone, A. Universal l^{-3} finite-size effects in the viscoelasticity of confined amorphous systems (2020). [2012.05149](https://doi.org/10.1103/2012.05149).

79. Ortiz-Young, D., Chiu, H.-C., Kim, S., Voitchovsky, K. & Riedo, E. The interplay between apparent viscosity and wettability in nanoconfined water. *Nat. Commun.* **4**, 2482, DOI: [10.1038/ncomms3482](https://doi.org/10.1038/ncomms3482) (2013).

80. Cerveny, S., Mallamace, F., Swenson, J., Vogel, M. & Xu, L. Confined water as model of supercooled water. *Chem. Rev.* **116**, 7608–7625, DOI: [10.1021/acs.chemrev.5b00609](https://doi.org/10.1021/acs.chemrev.5b00609) (2016). PMID: 26940794, <https://doi.org/10.1021/acs.chemrev.5b00609>.

81. Zaccone, A. & Trachenko, K. Explaining the low-frequency shear elasticity of confined liquids. *Proc. Natl. Acad. Sci.* **117**, 19653–19655, DOI: [10.1073/pnas.2010787117](https://doi.org/10.1073/pnas.2010787117) (2020). <https://www.pnas.org/content/117/33/19653.full.pdf>.
82. Marcano, D. C. *et al.* Improved synthesis of graphene oxide. *ACS nano* **4**, 4806–4814 (2010).
83. Paciaroni, A. *et al.* Fingerprints of amorphous icelike behavior in the vibrational density of states of protein hydration water. *Phys. review letters* **101**, 148104 (2008).
84. Richard, D., Ferrand, M. & Kearley, G. Lamp, the large array manipulation program. *J. Neutron Res* **4**, 33–39 (1996).
85. Plimpton, S. Fast parallel algorithms for short-range molecular dynamics. *J. Comput. Phys.* **117**, 1–19, DOI: <https://doi.org/10.1006/jcph.1995.1039> (1995).
86. Abascal, J. L. F. & Vega, C. A general purpose model for the condensed phases of water: Tip4p/2005. *The J. Chem. Phys.* **123**, 234505, DOI: [10.1063/1.2121687](https://doi.org/10.1063/1.2121687) (2005). <https://doi.org/10.1063/1.2121687>.
87. Kumar, P., Wikfeldt, K. T., Schlesinger, D., Pettersson, L. G. M. & Stanley, H. E. The boson peak in supercooled water. *Sci. Reports* **3**, 1980, DOI: [10.1038/srep01980](https://doi.org/10.1038/srep01980) (2013).

Supplementary information

Additional experimental data

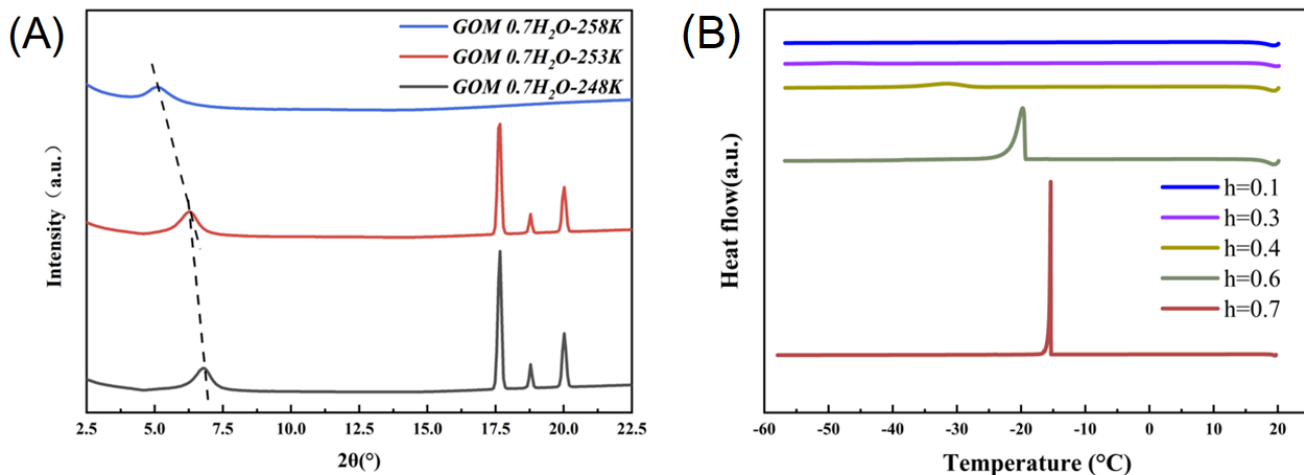


Figure 6. (A): The SAXS data of GOM with $h = 0.7$ at different temperatures, showing the characteristic peaks of the GOM layer spacing shift with the formation of ice. (B): The DSC result during cooling process for GOM sample with different hydration level.

In Fig.6 (A), the characteristic peak of the GOM sample layer spacing is shifting with the temperature decreasing and the formation of ice. This shows that as the temperature drops, the water confined in the GOM layers migrates to some voids or to the surface of GOM to form bulk crystalline ice. Therefore, the GOM layer spacing decreases significantly. So called the ice segregation process.^{68–70} As shown in Fig.6 (B), we made the DSC measurement for the samples with different hydration levels and no first-order transition was observed at $h = 0.3$ or below, but it appears at higher hydration levels, $h = 0.4$ and above. So we can note that in samples with water content of 0.3 and below, the crystalline ice cannot be formed, consistent with our SAXS results in Fig.3 (C). The ratio of the bulk ice and amorphous ice is calculated using the latent heat of first order phase transition of water.

Failure of the hard-wall boundary conditions

Let us consider a simple wave equation in a three-dimensional box of size $L_x \times L_y \times L_z$. For simplicity, and importantly not for any fundamental physical reason, such an equation is usually solved by assuming the so-called smooth hard-wall boundary conditions, namely that the displacement field vanishes on all the edges of the box. Under these assumptions, and neglecting the time dynamics of the wave-equation since irrelevant for our purposes, the solution is simply:

$$\phi(x, y, z) = \sin(k_x x) \sin(k_y y) \sin(k_z z) \quad (15)$$

supplemented by the following conditions:

$$\sin(k_x L_x) = \sin(k_y L_y) = \sin(k_z L_z) = 0 \quad (16)$$

which are immediately solved by:

$$k_x = i \frac{\pi}{L_x}, \quad k_y = j \frac{\pi}{L_y}, \quad k_z = k \frac{\pi}{L_z}, \quad (17)$$

with i, j, k integers.

The hard-wall boundary conditions have therefore two striking consequences. (I) the wave-vector is discrete and (II) there is a minimum wave-vector.

Going back to our experimental sample, there we can take safely $L_x, L_y \rightarrow \infty$. Nevertheless, this would still imply that $|k| = \sqrt{k_x^2 + k_y^2 + k_z^2}$ is bounded from below by:

$$|k| > \frac{\pi}{L} \quad (18)$$

where $L = L_z$ as in the main text.

If this argument were true, our theoretical explanation presented in the main text would be clearly invalid (see for example⁴⁸, where periodic boundary conditions were instead used in the simulations). Nevertheless, as we showed directly here using MD simulations, this is not the case and the smooth hard-wall boundary conditions do not apply to our system. As an immediate consequence, (I) our wave-vector is not discrete and (II) our wave-vector is not limited from below by π/L .

In Fig. 7, we calculated the longitudinal current correlation function and dispersion relation in the supercooled liquid slab. The wave-vector along the z direction k_z is fixed at $\sim 0.07 \text{ \AA}^{-1}$, which corresponds to $\frac{\pi}{2L}$, much below the minimal value allowed by hard-wall bcs. In Fig. 7 (A), we can clearly see that the peak position shifts to higher frequency with increasing $|k|$. This results suggest that a well-defined propagating mode exists also for values of k_z which are not allowed by the hard-wall bcs. In addition, we compare the dispersion relation for wavevector $k_z = 0.07 \text{ \AA}^{-1}$ with that for wavevector parallel to the xy plane in Fig. 7 (B). From there, we observe that two dispersion relations strongly overlap, meaning the dispersion relation is only related to the norm of the wave-vector $|k|$.

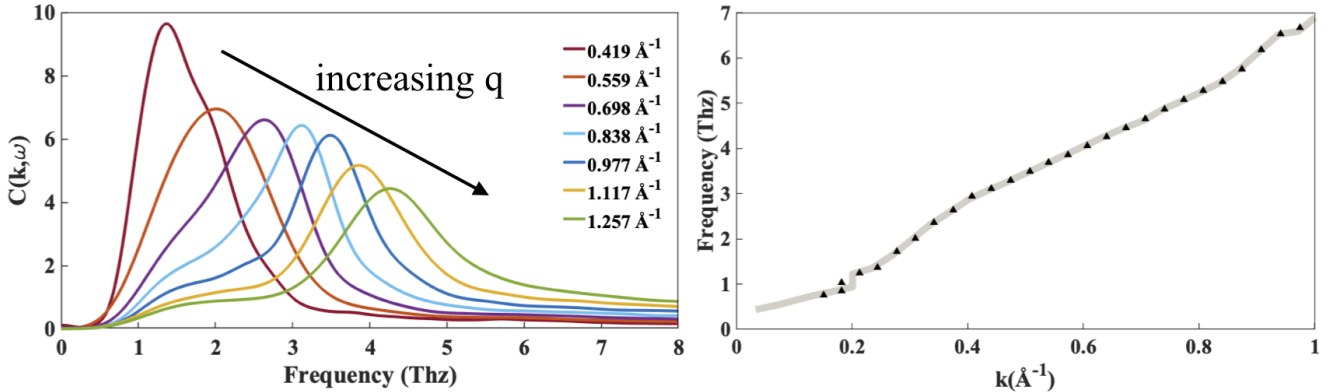


Figure 7. (A): The longitudinal current correlations spectrum at different k_x with fixed $k_z = 0.07 \text{ \AA}^{-1}$. The arrow indicates the motion of the intensity peak upon moving the wave-vector k_x . **(B):** The dispersion relation as a function of $|k|$. The grey line represents the dispersion relation with wavevector parallel to the xy plane. The black triangles represent the dispersion relation with wavevector $k_z = 0.07 \text{ \AA}^{-1}$.